


















Orbital-selective metal skin induced by alkali-metal-dosing Mott-insulating Ca_2RuO_4

Masafumi Horio^{1,2}[✉], Filomena Forte^{3,4}[✉], Denys Sutter², Minjae Kim^{5,6,7}, Claudia G. Fatuzzo², Christian E. Matt², Simon Moser^{8,9,10}, Tetsuya Wada¹, Veronica Granata⁴, Rosalba Fittipaldi^{3,4}, Yasmine Sassa¹¹, Gianmarco Gatti^{12,13}, Henrik M. Rønnow¹², Moritz Hoesch^{14,15}, Timur K. Kim¹⁴, Chris Jozwiak⁸, Aaron Bostwick⁸, Eli Rotenberg⁸, Iwao Matsuda¹, Antoine Georges^{5,6,13,16}, Giorgio Sangiovanni^{10,17}, Antonio Vecchione^{3,4}, Mario Cuoco^{3,4} & Johan Chang²

Doped Mott insulators are the starting point for interesting physics such as high temperature superconductivity and quantum spin liquids. For multi-band Mott insulators, orbital selective ground states have been envisioned. However, orbital selective metals and Mott insulators have been difficult to realize experimentally. Here we demonstrate by photoemission spectroscopy how Ca_2RuO_4 , upon alkali-metal surface doping, develops a single-band metal skin. Our dynamical mean field theory calculations reveal that homogeneous electron doping of Ca_2RuO_4 results in a multi-band metal. All together, our results provide evidence for an orbital-selective Mott insulator breakdown, which is unachievable via simple electron doping. Supported by a cluster model and cluster perturbation theory calculations, we demonstrate a type of skin metal-insulator transition induced by surface dopants that orbital-selectively hybridize with the bulk Mott state and in turn produce coherent in-gap states.

¹Institute for Solid State Physics, The University of Tokyo, Kashiwa, Chiba 277-8581, Japan. ²Physik-Institut, Universität Zürich, Winterthurerstrasse 190, CH-8057 Zürich, Switzerland. ³CNR-SPIN, I-84084 Fisciano, Salerno, Italy. ⁴Dipartimento di Fisica “E.R. Caianiello”, Università di Salerno, I-84084 Fisciano, Salerno, Italy. ⁵Collège de France, F-75231 Paris Cedex 05, France. ⁶Centre de Physique Théorique, Ecole Polytechnique, CNRS, Université Paris-Saclay, F-91128 Palaiseau, France. ⁷Korea Institute for Advanced Study, Seoul 02455, South Korea. ⁸Advanced Light Source (ALS), Berkeley, CA 94720, USA. ⁹Physikalisches Institut, Universität Würzburg, Würzburg 97074, Germany. ¹⁰Würzburg-Dresden Cluster of Excellence ct.qmat, Universität Würzburg, Würzburg 97074, Germany. ¹¹Department of Physics, Chalmers University of Technology, SE-412 96 Göteborg, Sweden. ¹²Institute of Physics, École Polytechnique Fédérale de Lausanne (EPFL), CH-1015 Lausanne, Switzerland. ¹³Department of Quantum Matter Physics, University of Geneva, 24 Quai Ernest-Ansermet, CH-1211 Geneva 4, Switzerland. ¹⁴Diamond Light Source, Harwell Campus, Didcot OX11 0DE, UK. ¹⁵Deutsches Elektronen-Synchrotron DESY, Notkestrasse 85, 22607 Hamburg, Germany. ¹⁶Center for Computational Quantum Physics, Flatiron Institute, 162 5th Avenue, New York, NY 10010, USA. ¹⁷Institut für Theoretische Physik und Astrophysik, Universität Würzburg, Würzburg 97074, Germany. ✉email: mhorio@issp.u-tokyo.ac.jp; filomena.forte@spin.cnr.it

Interface metallicity paves the way for two-dimensional fermionic gasses with interesting properties such as superconductivity^{1–3}. Insulators are building blocks for such interfaces. Upon doping (charge transfer), two-dimensional metals can occur at the interface between two insulators like LaAlO₃ and SrTiO₃^{4,5} or at the insulator–vacuum interface like the surface of SrTiO₃^{6,7}. Such metallic states confined at interfaces are broadly dubbed quantum well states. This term is used irrespectively of insulating nature (band or Mott insulators). For many spectroscopies, insulator–vacuum interfaces are interesting as they are directly accessible in contrast to buried⁸ insulator–insulator quantum wells. Doping of insulator–vacuum interfaces are often achieved by dosing with alkali metal atoms^{9–13}. Electrons from the alkali-metal layer can form a quantum-well state confined by vacuum and the band gap of the substrate. When the substrate band gap is sufficiently large, the metallic state can be strictly confined inside the alkali-metal overlayer¹¹. On the other hand, with significant energy and momentum overlap, the quantum well state will hybridize with the substrate and form a hybrid state^{10,12}. In this context, particularly interesting is the case of Mott insulators as a substrate. In contrast to the rigid band gap of band insulators, a Mott gap is maintained by a delicate balance between kinetic energy and electron correlation¹⁴. This in turn suggests that the interaction between the alkali metal and the electronic states of the Mott insulator could trigger the breakdown of the Mott state at the surface, leaving a hybrid quantum-well state.

Here we demonstrate—using photoemission spectroscopy—that alkali add-on atoms on Mott insulating Ca₂RuO₄ generates such a hybrid quantum well state. Independent of the chosen alkali-metal element (K, Rb, Cs), we observe a depletion of the lower-Hubbard-band (LHB) spectral weight and an evolution of the Ru core-level states as a function of doping, which are typical manifestations of a Mott breakdown^{15–17}. Eventually, a single-band metal emerges as a result of the interaction between the alkali-metal dopants and the Ca₂RuO₄ substrate. Our work reveals a type of orbital-selective surface metal–insulator transition induced through in-gap state formation generated by orbital hybridization between surface dopants and the Mott insulating substrate (schematically illustrated in Fig. 1).

Results

Electronic-structure evolution by alkali-metal dosing. Rb 4*p* core level spectroscopy and electronic band structure of Ca₂RuO₄ single crystals as a function of alkali-metal deposition are shown in Fig. 2a and b, respectively. Angle-resolved photoemission

spectroscopy (ARPES) spectra are recorded along the Γ –M direction. Before alkali-metal deposition, the electronic structure—shown in Fig. 2b, left panel—is consistent with previous reports^{15,18}. Around the Brillouin zone center, dispersive bands (2.5–0.5 eV) are observed and the non-dispersive LHB is located about ~1.7 eV below the Fermi level (E_F). Previously, the dispersive bands have been assigned predominately to the d_{xy} orbital and the LHB to the d_{xz}/d_{yz} orbitals^{15,18,19}. Upon dosing Rb, the whole structure is shifted downwards [Fig. 2b] and a Rb 4*p* core level peak develops [Fig. 2a]. By further dosing Rb, an in-gap state with an electron-like dispersion evolves from its band bottom. Whereas the low-energy spectral weight is initially negligible, the band extends with the increase of the Rb amount and finally produces finite spectral weight at E_F (See Supplementary Fig. 1). These changes occur qualitatively in the same manner irrespectively of the choice of alkali-metal dopants—see Fig. 2c, d for the case of K and Cs dosing.

Surface Mott breakdown in Ca₂RuO₄. Momentum-integrated energy distribution curves (EDCs) are plotted in Fig. 3a. Besides Ru 4*d*-derived states including LHB, O 2*p* states are identified at ~3.2 eV below E_F ¹⁸. Upon Rb dosing, the O 2*p* peak moves to higher binding energy until the shift saturates at ~0.3 eV, followed by a slight shift backward. While Ru ions could change their valency when doped with electrons, oxygen ions should remain chemically unperturbed. The O 2*p* peak position thus serves as a measure of the chemical-potential shift as demonstrated by previous studies of oxide materials^{16,20}. In Fig. 3b, we align the O 2*p* peak position to compensate for the chemical-potential shift and unravel, in this fashion the intrinsic lower-energy structures. The total spectral intensities, within the displayed energy window, are normalized to eliminate attenuation effects from the Rb overlayer. After these data treatments, a prominent decay of LHB intensity (magenta-shaded region) is observed concomitantly with the growth of near- E_F spectral weight (green-shaded region)—see Fig. 3c. In contrast to the drastic changes in the spectral weight, the position of the LHB is essentially independent of alkali dosing [Fig. 3d]. This suggests that the size of the Mott gap is unaffected by alkali-metal dosing even though the chemical potential moves inside the gap. Instead of the shrinkage of the gap size, the collapse of the Mott gap is driven by the spectral-weight loss in the Hubbard bands.

Core-level structure. The Ru 3*d* core levels, probed by x-ray photoemission spectroscopy (XPS), provide insights into the dosing-induced metallic surface state. In Mott insulating

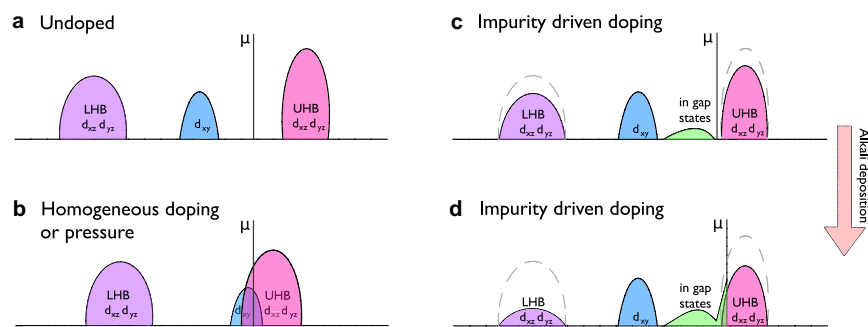


Fig. 1 Mott-insulator re-metallization schemes of Ca₂RuO₄. **a** Schematic representation of the Ca₂RuO₄ band-Mott insulating structure⁴⁵. LHB and UHB denote the lower and upper Hubbard bands, respectively. In the short *c*-axis phase, the d_{xy} band is fully occupied whereas the half-filled d_{xz}/d_{yz} orbitals are Mott insulating forming LHB and UHB. **b** Homogeneous bulk doping, and chemical or applied pressure are expected to generate a multi-band metal that involves all the t_{2g} orbitals. **c** Impurity electron doping, from surface alkali-metal deposition, turns out to generate in-gap states through hybridization with the Mott insulating d_{xz}/d_{yz} orbitals. The in-gap states emerge in conjunction with partial spectral weight suppression of the Hubbard bands (indicated by dashed gray lines). **d** Re-metallization upon crossing a certain threshold of impurity doping level. Due to the orbital-selective hybridization between surface dopants and the high-energy incoherent excitations, a single-band metal is formed.

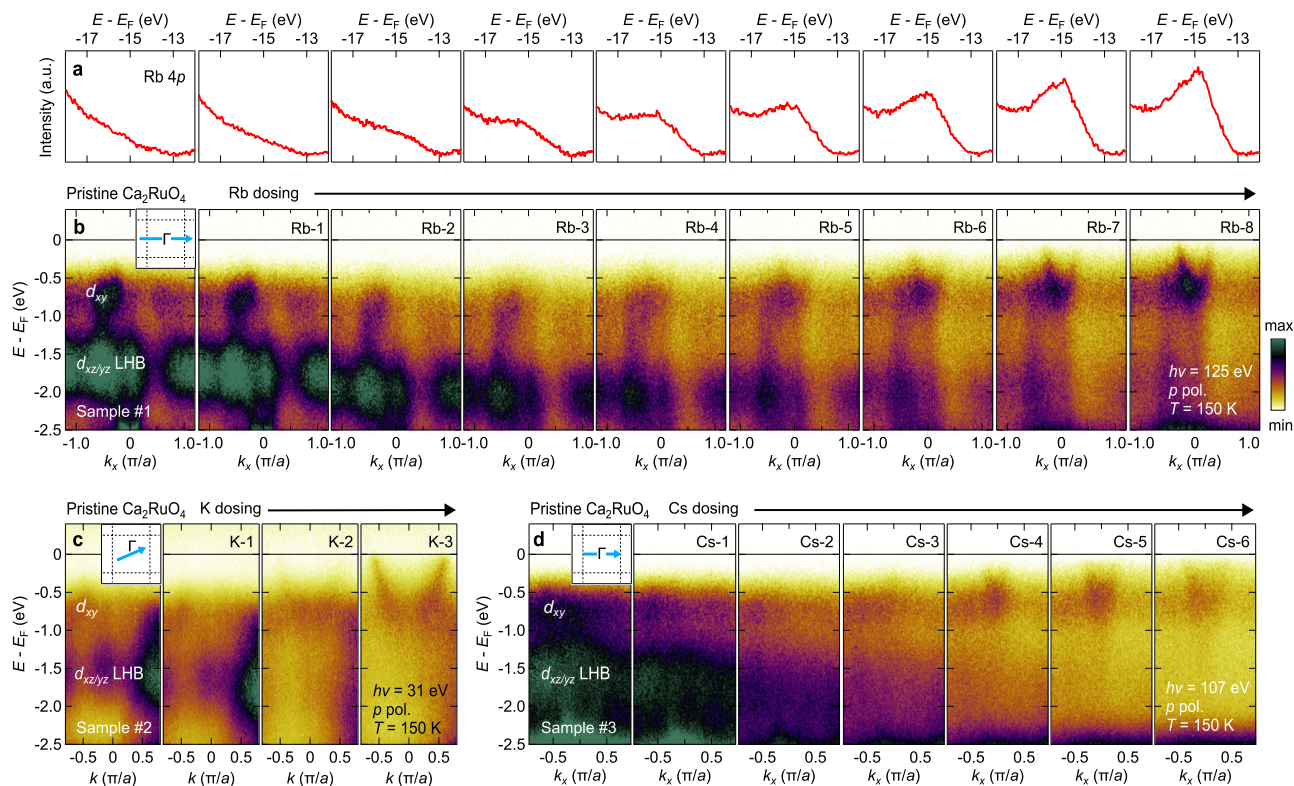


Fig. 2 Surface electronic structure evolution of Ca_2RuO_4 by alkali-metal dosing. **a, b** Rb 4p energy distribution curves (EDCs) and valence-band energy distribution maps (EDMs), respectively, recorded at the temperature of $T = 150$ K with dosing Rb in incremental steps. p -polarized 125-eV incident light is used. The momentum cut is indicated in the inset of the leftmost panel. The color bar quantifies photoemission intensity. **c, d** EDMs recorded with dosing K and Cs using p -polarized light of $h\nu = 31$ and 107 eV, respectively. Similar changes as the Rb case are observed.

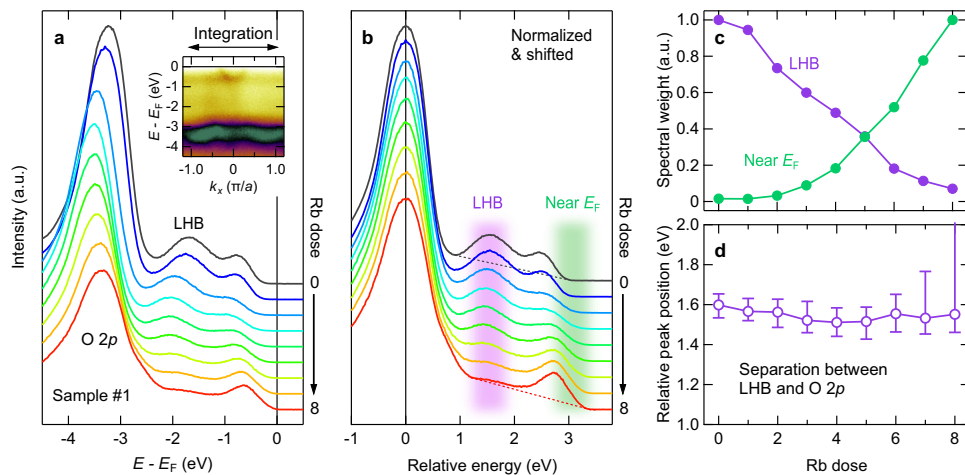


Fig. 3 Surface Mott breakdown in Ca_2RuO_4 . **a** Valence-band energy distribution curves (EDCs) versus energy relative to E_F plotted in the order of Rb deposition levels. Spectra are given arbitrary vertical offsets for a visibility purpose. The inset indicates the momentum window for integration. **b** Valence band EDCs aligned to the O 2p peak position and normalized to the total intensity in the displayed energy region. **c** Spectral weight of the lower Hubbard band (LHB) and the near- E_F part integrated within the magenta and green shaded regions, respectively, in **(b)**. The LHB spectral weight is estimated after subtracting a tangential linear background shown by dotted lines in **(b)**. The weight has been normalized to the maximum values. **d** The position of LHB with respect to the O 2p peak position plotted as a function of the Rb deposition sequence. The error bar is determined from intensity variation around the peak surpassing the noise level.

Ca_2RuO_4 and $\text{Y}_2\text{Ru}_2\text{O}_7$, the Ru $3d$ peak is composed of a single set of spin-orbit-split peaks ($3d_{5/2}$ and $3d_{3/2}$) as shown in Fig. 4a, b. Isovalent Bi substitution for Y¹⁷ drives a band-width-controlled Mott transition, and the resulting metallic state of $\text{Bi}_2\text{Ru}_2\text{O}_7$ yields splittings within the $3d_{5/2}$ and $3d_{3/2}$ levels [Fig. 4b]. It has been proposed that the low-energy peak stems from a final state where core holes are screened by conduction electrons¹⁷. Upon

Cs dosing of Ca_2RuO_4 , a very similar splitting of the core levels is observed [Fig. 4a]—suggesting the emergence of conduction electrons with Ru character.

Surface metallic state. Having tracked in detail the evolution of the electronic structure by alkali-metal dosing, we now focus on the character of the created metallic state. To embed the momentum-

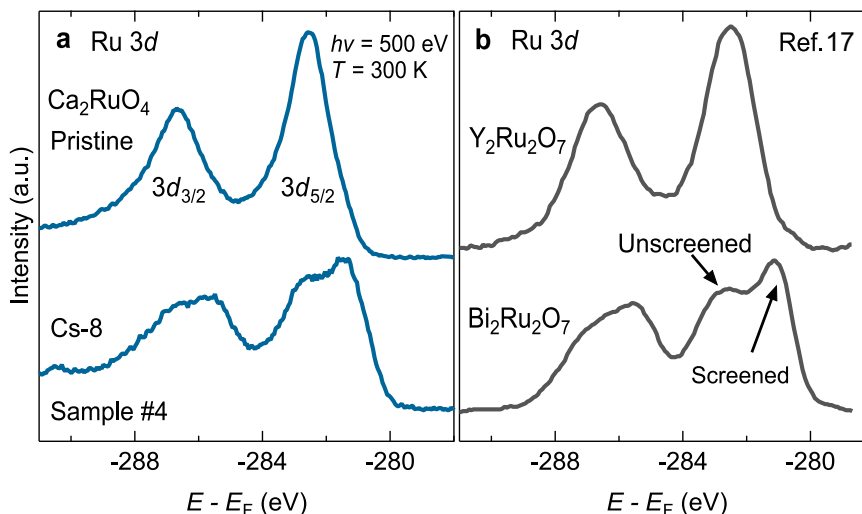


Fig. 4 Evolution of core levels. **a** Ru 3d spectra of Ca_2RuO_4 measured by x-ray photoemission spectroscopy (XPS) before and after dosing Cs at 300 K. **b** Ru 3d XPS spectra of Mott-insulating $\text{Y}_2\text{Ru}_2\text{O}_7$ and metallic $\text{Bi}_2\text{Ru}_2\text{O}_7$ from ref. ¹⁷ with the binding energy aligned to that of Ca_2RuO_4 .

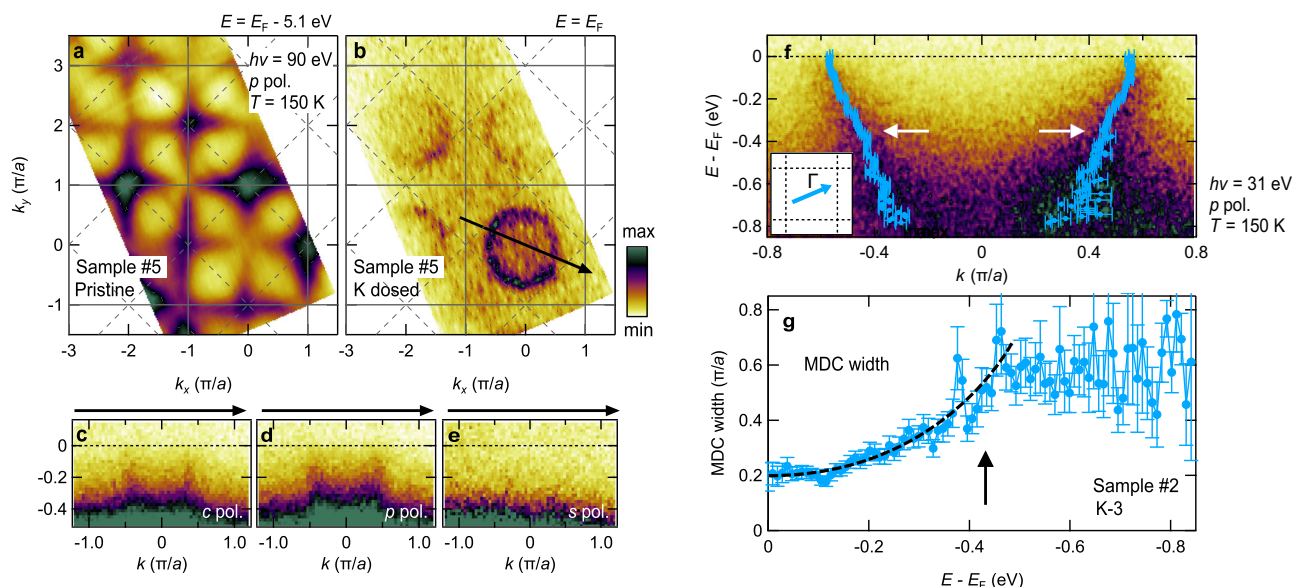


Fig. 5 Metallic surface state of alkali-metal dosed Ca_2RuO_4 . **a** Constant-energy map of pristine Ca_2RuO_4 at $E = E_F - 5.1$ eV recorded with $h\nu = 90$ eV, p -polarized photons at the temperature of $T = 150$ K. The oxygen bands draw a periodic structure. Overlaid gray solid and dashed squares represent Brillouin zones in the tetragonal and orthorhombic notations, respectively. **b** Fermi surface after K dosing for 10 min at 6.5 Å. The color bar quantifies photoemission intensity. **c–e** Energy distribution maps (EDMs) recorded with circular, p , and s polarization, respectively, along the cut indicated in **(b)**. The band becomes indiscernible when measured with s -polarized light. **f** EDM of the K-dosed state [identical to K-3 in Fig. 2c] overlaid with momentum-distribution-curve (MDC) peak positions, recorded with $h\nu = 31$ eV, p -polarized photons along the cut shown in the inset. **g** MDC full width at half maximum averaged over the two branches. The dashed curve indicates the low-energy dependence to guide the eye. Kinks in the MDC peak position and width are indicated by arrows. Error bars are based on the standard deviation of the fitting.

resolved photoemission signal into the Brillouin zone of Ca_2RuO_4 , we use the constant-energy map intersecting oxygen bands¹⁸—see Fig. 5a. Then, Fermi surface after metallization is mapped out in the same momentum regions. The resulting map [Fig. 5b] reveals circular Fermi surfaces in accordance with the tetragonal Brillouin zone. The bulk crystal structure of Ca_2RuO_4 is orthorhombic. Numerous ARPES studies have accumulated evidence that the potential of orthorhombic distortion is strong enough to cause band folding^{21–25}. The absence of band folding suggests that the metallic surface state is not strictly confined in the Ca_2RuO_4 crystal. The spectral intensity of the electron-like band composing the Fermi surface depends strongly on incident light polarization [Fig. 5c–e] and is suppressed with s -polarized light. In contrast, the

band is visible with p -polarized light irrespective of the azimuthal angle of the mirror plane [see also Fig. 2b, c]. The band therefore possesses in-plane even character. As shown in Fig. 5f, the metallic band exhibits a kink (sudden change of band velocity) at ~ 0.4 eV below E_F (see also Supplementary Fig. 2 for detailed analysis). This is also evidenced by a saturation of the momentum distribution curve (MDC) linewidth [Fig. 5g].

Discussion

Our main observation is a metallization of Ca_2RuO_4 upon application of alkali-metal atoms. A central question is whether this quantum well state is a hybrid state between alkali metals and Ca_2RuO_4 . We address this question by inspecting: (i) the spectral

weight of the LHB, (ii) the Ru-core levels, and (iii) the self-energy effects of the induced quantum well state.

(i) Mono-, bi-, and tri-layer alkali-metal deposition have been reported^{9,26} on Sr_2IrO_4 and Sr_2RuO_4 . Due to the large inelastic mean free path of alkali metals²⁷, bulk bands are observed through the alkali-metal layers in both cases. The observation of drastic LHB suppression (Fig. 3) is thus intrinsic and not an artifact of an alkali-metal overlayer. With few exceptions²⁸, spectral weight suppression of the Hubbard bands is associated with quasi-particle formation near the chemical potential^{16,29}. This is consistent with our observation of a fading Hubbard band being replaced by a valence band as a function of alkali-metal dosing.

(ii) Also the Ru core level [Fig. 4a] is modified by alkali-metal deposition. The simplest possibility of lower-energy satellite in the Ru $3d$ peak is a Ru^{3+} component created by doping Ru^{4+} with an electron. However, the intense low-energy peak translates into more than 0.6 electrons doped per Ru atom. This value is unrealistic as previous alkali-metal adsorption studies on oxides found at most ~ 0.15 electrons doped per atom^{9,13,16,26}. Instead, such an intense low-energy satellite peak, which appears upon metallization of Mott insulators like cuprates^{30,31} and ruthenates^{17,32}, has been associated with a final state where core holes are efficiently screened by conduction electrons. The change induced by alkali-metal dosing [Fig. 4a] thus suggests the emergence of itinerant electrons with, at least partially, the Ru $3d$ character. We note that the linewidth of other core levels such as Ca $3p$ is essentially insensitive to dosing of alkali atoms [see Supplementary Fig. 3] suggesting that the Ru $3d$ transformation is intrinsic.

(iii) Finally, the kink witnessed both in the band dispersion [Fig. 5f] and MDC linewidth [Fig. 5g] of the metallic band suggests strong self-energy effects. The energy scale of 0.4 eV is incompatible with electron-phonon interactions and rather points to electron-electron interactions. In fact, such high-energy kinks have been widely observed in strongly correlated systems like cuprates^{33,34} and ruthenates³⁵, and interpreted as a manifestation of many-body self-energy effects. The kink, therefore, suggests substantial electron correlations induced by substrate Ru orbitals. Such correlation effects are not expected (or reported) for a purely alkali-metal quantum-well states¹¹.

Based on observations (i)–(iii), we conclude that the induced metallic state involves an interaction between alkali-metal atoms and Ca_2RuO_4 .

So far, bulk electron doping of Ca_2RuO_4 has been achieved only by substituting La or Pr for Ca^{36–38}. This substitution inevitably involves chemical pressure. As a similar metal-insulator transition is observed with isovalent Sr substitutions³⁹, chemical pressure rather than doping is most likely the metallization mechanism of La/Pr doping. In all cases, the resulting metallic state comprises multiple Fermi surfaces—composed of almost evenly filled d_{xz} , d_{yz} , and d_{xy} orbitals^{15,24}. These electronic structures are realistically captured by dynamical mean-field theory (DMFT) calculations, which take into account both electronic structure and strong correlations (self-energy) effects^{15,24}. In the present surface-dosed case, it is unclear whether the transition involves c -axis changes. We therefore performed DMFT calculations for the short c -axis phase to evaluate genuine electron-doping effects. As shown in Supplementary Fig. 4, electron doping again leads to the formation of multiple Fermi surface sheets (see also Supplementary Note 1). This demonstrates that alkali metal dosing does not correspond to the standard theoretical description of homogeneous electron doping [Fig. 1b]. Surface re-metallization due to Coulomb screening is also expected to yield a multiband metal.

Inspection of the initial stage of the band-structure evolution by alkali-metal dosing [Fig. 2b–d] indicates no detectable spectral weight accumulation at E_F . This is in direct contrast to electron

doping of Mott insulating cuprates^{16,40}, and is an indication that the charge transfer of the alkali valence electrons to the upper Hubbard band (UHB) is not complete. This result suggests a covalent nature of bonding with partial charge transfer to the Ru bands. Alkali-metal s electrons are thus not directly injected into the UHB. Instead, they reside on localized impurity states with pinned chemical potential within the gapped region. Such impurity states can hybridize with the Ru d orbitals provided sufficient spacial overlap and symmetry compatibility. Linear combination of d_{xz} and d_{yz} orbitals (with even parity) is the most obvious candidate for such hybridization. The formation of interfacial bonding states between surface-dosed alkali-metal s and transition-metal d orbitals has been frequent observation in previous photoemission studies^{12,41–44}.

We therefore evaluated the orbital-dependent spectral function via exact diagonalization of a cluster made of one Ru site and one impurity level. The model consists of the local interaction terms at the Ru and the impurity sites, and the kinetic term t among the d_{xz}/d_{yz} and the impurity orbitals. The following choices are made for the parameters: $U = 2$ eV, $J = 0.5$ eV, $\Delta_{\text{CF}} = 0.3$ eV, $\lambda = 0.075$ eV, $U_I = 1$ eV^{18,45,46}, where U is the Coulomb interaction between Ru $4d$ electrons, J is the Hund's coupling, Δ_{CF} is crystal-field splitting within the t_{2g} sector, λ is spin-orbit coupling, and U_I is the Coulomb interaction within the impurity level. We assume that the impurity level lies close to the bottom of the UHB and we mimic the increase of the doping concentration by increasing the parameter t , allowing more hybridization between the Ru d_{xz}/d_{yz} and impurity level. As shown in Fig. 6a, b, the initial change with small t is the shift of chemical potential to accommodate the impurity level. Upon increasing hybridization, the spectral weight of the d_{xz}/d_{yz} LHB located at $E \sim E_F - 2$ eV is significantly suppressed and instead a new state with a mixed character of Ru d_{xz}/d_{yz} and impurity s appears near E_F [Fig. 6c]. Further increase of t results in accumulating the spectral weight of this bonding state [Fig. 6d]. The overall changes are in good agreement with the experiment. We can provide a qualitative interpretation of the cluster calculations by analyzing the multiplet eigenstates and electronic transitions for the Ru and the alkali impurity state at the ionic level. A detailed analysis is reported in Supplementary Figs. 5, 6, Supplementary Notes 2 and 3. The ground state is built up as a quantum superposition of local $|d, s\rangle$ configurations with a fully occupied d_{xy} orbital, due to the extreme flattening of the Ru-O octahedra. Assuming a selective hybridization among the s level and d_{xz}/d_{yz} doublet, this superposition involves $|d^4, s^1\rangle$ and $|d^5, \bar{s}\rangle$ states. Thus, two spectral features can be obtained via the removal of one electron from the d_{xz}/d_{yz} doublet, which arise from an electronic transition to the $|d^3 s^1\rangle$ and $|d^4, \bar{s}\rangle$ state, respectively. While the former contributes to the weight of the LHB, the latter corresponds to the in-gap states and is expected to increase its spectral weight as the deposition sequence goes on.

The effects of such orbital-selective hybridization mechanism on the extended system are schematized in Fig. 1d. Here we show that the Mott breakdown takes place due to the progressive depletion of the d_{xz}/d_{yz} LHB and consequent filling of the in gap impurity-driven states. It is worthwhile to notice that such mechanism has side effects also on the d_{xy} band through Hund's coupling. Due to the covalent nature of the ground state, the spectral weight associated to the d_{xy} removal states spreads out between several allowed electronic transitions at slightly higher binding energies (See Supplementary Figs. 5, 6, and Supplementary Note 3 for details), depleting the d_{xy} spectral weight in the low energy state (Fig. 6c) as seen experimentally (Fig. 2). After sufficient dosing (Rb-8 in Fig. 2), ARPES reveals broad spectral weight around the binding energy of 0.5–1 eV, spreading over a wide momentum range. Referring to the theoretical prediction (Fig. 6d), this electronic state is likely of d_{xy} origin.

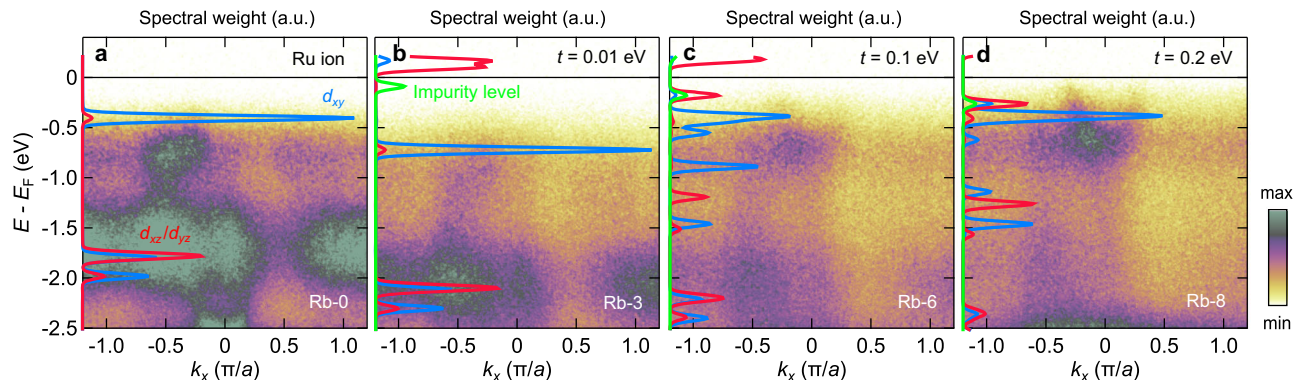


Fig. 6 Cluster analysis of Ca_2RuO_4 interacting with an alkali-metal impurity level. **a–d** Spectral function calculated for Ru ion, $t = 0.01$ eV, $t = 0.1$ eV, and $t = 0.2$ eV, respectively, where t represents the hybridization term. Superimposed are energy distribution maps from Fig. 2b with Rb deposition sequences as indicated. The color bar quantifies photoemission intensity.

Finally, we notice that the orbital-selective hybridization can naturally lead to the formation of a single-sheet Fermi surface that is not reproduced by the homogeneous doping picture. The symmetry analysis of the metallic state (Fig. 5) is also compatible with the in-plane even character of the bonding state. To further explore compatibility with the observation of a single Fermi surface sheet with free-electron-like dispersion, we combined the cluster calculation with cluster perturbation theory (CPT). The latter uses exact diagonalization of small clusters to construct a strong-coupling perturbation theory for the lattice problem⁴⁷ (see Supplementary Note 4). Even though this approach represents a simplification of the complex physics characterizing the large dopant regime, it allows to determine the Fermi surfaces to be compared to our experimental results. In particular, we are interested in the evolution with the alkali-metal content of the low-energy features corresponding to the in-gap states. In the atomic regime, as demonstrated in the cluster calculation, the in-gap localized states are mainly made of s - and d_{xz}/d_{yz} states with a relative charge distribution dictated by the hybridization and the multiplet configurations at the Ru sites. These localized states can overlap along the Ru-O-Ru bond directions. In order to understand the formation of the Fermi pocket as due to the hybridization of the s -states with the Ru d -bands, it is particularly instructive to consider the limit with no direct overlap between the s -states. In this case, the effective mass of the s -state is due to the hybridization through the mixing with the Ru d -states across the Mott gap. As shown in Fig. 7a, b, we observe that the impurity level acquires an effective mass with a dispersion that substantially follows that of the d_{xz}/d_{yz} bands, due to the local hybridization. Since the d_{xz} and d_{yz} states have a quasi 1D electronic dispersion of the type $\cos k_x$ and $\cos k_y$, respectively, electrons in the s -state can propagate both along the x and y directions in the lattice. As a consequence of the orbital hybridization, the effective acquired dispersion of the s -state will have the following general structure $\epsilon_s(k_x, k_y) = -2\tilde{t}(\cos k_x + \cos k_y)$. Here, due to the correlated nature of the hosting electronic states, the effective hopping amplitude \tilde{t} depends on the Coulomb interaction and the spin-orbit coupling at the Ru site as well as on the electron density of the impurity level. Taking into account the form $\epsilon_s(k_x, k_y)$ of the dispersion close to the Fermi energy, the resulting Fermi pocket is isotropic as shown in Fig. 7c, d. Due to the hybridization among the impurity s - and the Ru d_{xz}/d_{yz} states, the emerging Fermi pocket for the s -state has also a non-vanishing spectral weight projected on the d_{xz} and d_{yz} orbital configurations. The displayed Fermi surface for the concomitant projection on both d_{xz} and d_{yz} [Fig. 7c] thus has the same profile as that for the s -states, even though the projection on the single

orbital configuration (d_{xz} or d_{yz}) would yield a Fermi line that is anisotropic and reflects the dominant 1D like character of the d_{xz} and d_{yz} bands. This result is confirming that our orbital selective model supports the formation of a single-sheet isotropic Fermi pocket.

The analysis has been performed for a representative case for the set of parameters used for the single site cluster calculation. Small variations do not affect the qualitative character of the Fermi pocket. The overall outcome is compatible with our experimental observation. We conclude that this scenario provides a novel type of surface Mott-insulator to metal transition realized through chemical doping. Note that a metallic in-gap state can also emerge by directly injecting carriers to the Hubbard bands^{16,48}. However, the present single-band in-gap state is incompatible with such direct carrier doping and instead suggests the orbital-selective formation of covalent bonds.

Due to the reduced coordination at surfaces, correlated systems have the opposite tendency, namely that of spontaneously forming a skin with suppressed conductivity. This has been observed and discussed in various oxides such as vanadates^{49–51}, cuprates³⁰, and ruthenates^{52,53}. The present work demonstrates the opposite case where dosed alkali metals increase surface hopping channels and produces a metallic skin on the Ca_2RuO_4 Mott insulating state. Although the multiband Mott insulating state of Ca_2RuO_4 is rather unique in nature, similar physics could be realized in other systems. Typical ingredients would be quasi-two-dimensional materials with Mott bands composed of inter-layer directed orbitals (p_z , d_z or d_{xz}) and moderate electron correlation. These criteria are uniquely satisfied in Ca_2RuO_4 . The Mott bands have predominately $4d_{xz}/d_{yz}$ character and the moderate correlation strength makes hybridization with deposited alkali-metal electrons possible.

Methods

Sample preparation and photoemission experiments. High-quality Ca_2RuO_4 single crystals were grown by the flux-feeding floating-zone method^{54,55}. ARPES measurements were carried out at the MAESTRO and I05 beamlines at Advanced Light Source and Diamond Light Source, respectively, at 150 K in the insulating short c -axis phase. Photon energy was varied in the range of 30–130 eV with energy resolution better than 50 meV. Presented ARPES data are recorded either using s -, p -, or circularly polarized light, with s and p denoting odd and even parity with respect to the photoemission mirror plane, respectively. XPS measurements were conducted at BL07LSU of SPring-8 at 300 K and 500 eV of incident photon energy. Samples #1–#3 and #5 were measured with ARPES and sample #4 with XPS. For all the

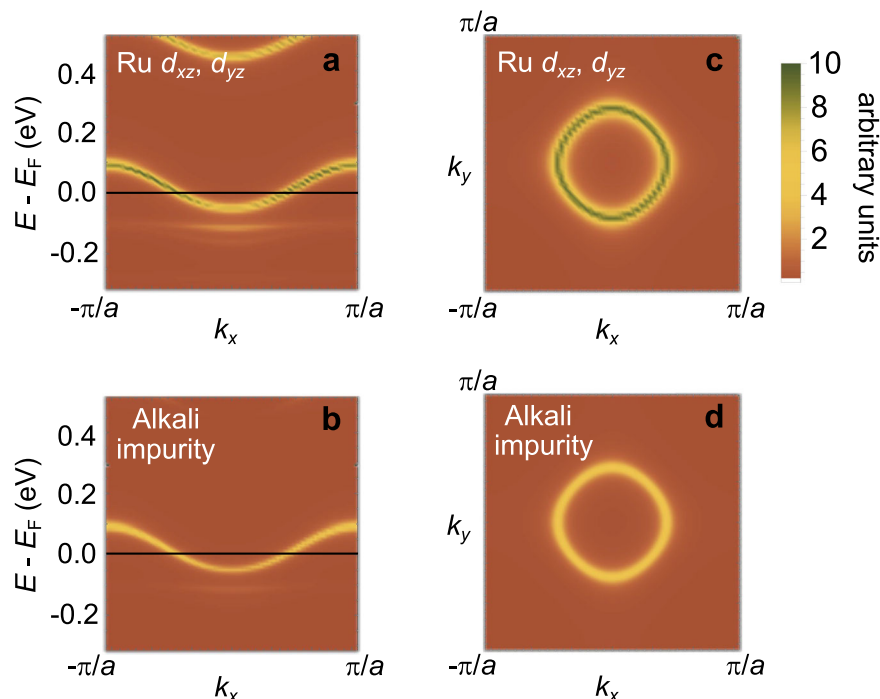


Fig. 7 Cluster perturbation theory analysis of the single-sheet Fermi surface. Electronic dispersions yielded by cluster perturbation theory calculations at $k_y = 0$ by varying k_x in the range $[-\pi, \pi]$ for the bands (a) arising from the Ru d_{xz}/d_{yz} orbitals and (b) from the impurity s -state at the alkali site. Black lines identify the Fermi level E_F . The color bar quantifies the spectral function. Fermi pocket of the (c) Ru d_{xz}/d_{yz} bands and (d) impurity band. The corresponding Fermi lines indicate the occurrence of an electron pocket centered at Γ . The spectral weight of the pocket is made of hybridized d_{xz}/d_{yz} and s bands. The computation refers to an electronic configuration with vanishing direct hybridization between the impurity states on nearest neighbors. The dispersion of the impurity s -state is yielded through the local hybridization with the Ru d -orbitals and the Ru-Ru effective charge transfer.

photoemission measurements, samples were cleaved in situ using the top-post method. SAES Getter dispensers were used to evaporate K, Rb, or Cs onto the Ca_2RuO_4 surface in incremental steps. Unless otherwise stated, one dose corresponds to evaporation of K, Rb, and Cs for respectively 40, 30, and 30 s with a filament current of 6.6, 6.4, and 8.3 Ampere. Note that Cs dosing for the ARPES and XPS measurements were done at different instruments and hence the dose unit is not exactly equivalent. No detectable charging was observed when varying the photon flux as long as the temperature was kept above 150 K. The tetragonal notation with $a = 3.80 \text{ \AA}$ is used to display ARPES data.

Data availability

The data that support the findings of this study are available from the corresponding author upon reasonable request.

Received: 15 June 2023; Accepted: 19 October 2023;

Published online: 06 November 2023

References

- Cavaglia, A. D. et al. Electric field control of the $\text{LaAlO}_3/\text{SrTiO}_3$ interface ground state. *Nature* **456**, 624–627 (2008).
- Kim, Y. K., Sung, N. H., Denlinger, J. D. & Kim, B. J. Observation of a d-wave gap in electron-doped Sr_2IrO_4 . *Nat. Phys.* **12**, 37–41 (2016).
- Liu, C. et al. Two-dimensional superconductivity and anisotropic transport at KTaO_3 (111) interfaces. *Science* **371**, 716–721 (2021).
- Liu, C. et al. Tunable superconductivity and its origin at KTaO_3 interfaces. *Nat. Commun.* **14** <https://doi.org/10.1038/s41467-023-36309-2> (2023).
- Reyren, N. et al. Superconducting interfaces between insulating oxides. *Science* **317**, 1196–1199 (2007).
- Santander-Syro, A. F. et al. Two-dimensional electron gas with universal subbands at the surface of SrTiO_3 . *Nature* **469**, 189–193 (2011).
- Moser, S. et al. Tunable polaronic conduction in anatase TiO_2 . *Phys. Rev. Lett.* **110**, 196403 (2013).
- Woerle, J. et al. Electronic band structure of the buried SiO_2/SiC interface investigated by soft x-ray ARPES. *Appl. Phys. Lett.* **110**, 132101 (2017).
- Kim, Y. K. et al. Fermi arcs in a doped pseudospin-1/2 Heisenberg antiferromagnet. *Science* **345**, 187–190 (2014).
- Alidoust, N. et al. Observation of monolayer valence band spin-orbit effect and induced quantum well states in MoX_2 . *Nat. Commun.* **5**, 4673 (2014).
- Eknapakul, T. et al. Nearly-free-electron system of monolayer Na on the surface of single-crystal HfSe_2 . *Phys. Rev. B* **94**, 201121 (2016).
- Akikubo, K. et al. Observation of an e_g -derived metallic band at the Cs/SrTiO_3 interface by polarization-dependent photoemission spectroscopy. *Thin Solid Films* **603**, 149–153 (2016).
- Yukawa, R. et al. Control of two-dimensional electronic states at anatase $\text{TiO}_2(001)$ surface by K adsorption. *Phys. Rev. B* **97**, 165428 (2018).
- Imada, M., Fujimori, A. & Tokura, Y. Metal-insulator transitions. *Rev. Mod. Phys.* **70**, 1039–1263 (1998).
- Riccò, S. et al. In situ strain tuning of the metal-insulator-transition of Ca_2RuO_4 in angle-resolved photoemission experiments. *Nat. Commun.* **9**, 4535 (2018).
- Hu, C. et al. Momentum-resolved visualization of electronic evolution in doping a Mott insulator. *Nat. Commun.* **12**, 1356 (2021).
- Kim, Hyeong-Do, Noh, Han-Jin, Kim, K. H. & Oh, S.-J. Core-Level X-ray photoemission satellites in ruthenates: a new mechanism revealing the Mott transition. *Phys. Rev. Lett.* **93**, 126404 (2004).
- Sutter, D. et al. Hallmarks of Hund's coupling in the Mott insulator Ca_2RuO_4 . *Nat. Commun.* **8**, 15176 (2017).
- Curcio, D. et al. Current-driven insulator-to-metal transition without Mott breakdown in Ca_2RuO_4 . *Phys. Rev. B* **108** <https://doi.org/10.1103/PhysRevB.108.L161105> (2023).
- Shen, K. M. et al. Missing quasiparticles and the chemical potential puzzle in the doping evolution of the cuprate superconductors. *Phys. Rev. Lett.* **93**, 267002 (2004).
- Damascelli, A. et al. Fermi surface, surface states, and surface reconstruction in Sr_2RuO_4 . *Phys. Rev. Lett.* **85**, 5194–5197 (2000).
- Tamai, A. et al. Fermi surface and van Hove singularities in the itinerant metamagnet $\text{Sr}_3\text{Ru}_2\text{O}_7$. *Phys. Rev. Lett.* **101**, 026407 (2008).
- Liu, Y., Nair, H. P., Ruf, J. P., Schlom, D. G. & Shen, K. M. Revealing the hidden heavy Fermi liquid in CaRuO_3 . *Phys. Rev. B* **98**, 041110 (2018).

24. Sutter, D. et al. Orbital selective breakdown of Fermi liquid quasiparticles in $\text{Ca}_{1.8}\text{Sr}_{0.2}\text{RuO}_4$. *Phys. Rev. B* **99**, 121115 (2019).
25. Horio, M. et al. Electronic reconstruction forming a C_2 -symmetric Dirac semimetal in $\text{Ca}_3\text{Ru}_2\text{O}_7$. *npj Quantum Mater.* **6**, 29 (2021).
26. Kyung, W. et al. Electric-field-driven octahedral rotation in perovskite. *npj Quantum Mater.* **6**, 5 (2021).
27. Smith, N. V., Wertheim, G. K., Andrews, A. B. & Chen, C.-T. Inelastic electron mean free paths in the alkali metals: effect of the empty d bands. *Surf. Sci.* **282**, L359–L363 (1993).
28. Zhou, X. et al. Angle-resolved photoemission study of the Kitaev candidate α - RuCl_3 . *Phys. Rev. B* **94**, 161106 (2016).
29. Eskes, H., Meinders, M. B. J. & Sawatzky, G. A. Anomalous transfer of spectral weight in doped strongly correlated systems. *Phys. Rev. Lett.* **67**, 1035–1038 (1991).
30. Taguchi, M. et al. Evidence for suppressed screening on the surface of high-temperature $\text{La}_{2-x}\text{Sr}_x\text{CuO}_4$ and $\text{Nd}_{2-x}\text{Ce}_x\text{CuO}_4$ superconductors. *Phys. Rev. Lett.* **95**, 177002 (2005).
31. Horio, M. et al. Electronic structure of Ce-doped and -undoped Nd_2CuO_4 superconducting thin films studied by hard X-ray photoemission and soft X-ray absorption spectroscopy. *Phys. Rev. Lett.* **120**, 257001 (2018).
32. Cox, P. A., Eggedell, R. G., Goodenough, J. B., Hamnett, A. & Naish, C. C. The metal-to-semiconductor transition in ternary ruthenium (IV) oxides: a study by electron spectroscopy. *J. Phys. C: Solid State Phys.* **16**, 6221–6239 (1983).
33. Xie, B. P. et al. High-energy scale revival and giant kink in the dispersion of a cuprate superconductor. *Phys. Rev. Lett.* **98**, 147001 (2007).
34. Chang, J. et al. When low- and high-energy electronic responses meet in cuprate superconductors. *Phys. Rev. B* **75**, 224508 (2007).
35. Iwasawa, H. et al. High-energy anomaly in the band dispersion of the ruthenate superconductor. *Phys. Rev. Lett.* **109**, 066404 (2012).
36. Fukazawa, H. & Maeno, Y. Filling control of the Mott insulator Ca_2RuO_4 . *J. Phys. Soc. Jpn.* **70**, 460–467 (2001).
37. Cao, G. et al. Ground-state instability of the Mott insulator Ca_2RuO_4 : impact of slight La doping on the metal-insulator transition and magnetic ordering. *Phys. Rev. B* **61**, R5053–R5057 (2000).
38. Pincini, D. et al. Tuning of the Ru^{4+} ground-state orbital population in the $4d^4$ Mott insulator Ca_2RuO_4 achieved by La doping. *Phys. Rev. B* **99**, 075125 (2019).
39. Nakatsuji, S. & Maeno, Y. Quasi-two-dimensional Mott transition system $\text{Ca}_{2-x}\text{Sr}_x\text{RuO}_4$. *Phys. Rev. Lett.* **84**, 2666–2669 (2000).
40. Armitage, N. P. et al. Doping dependence of an n -type cuprate superconductor investigated by angle-resolved photoemission spectroscopy. *Phys. Rev. Lett.* **88**, 257001 (2002).
41. Soukassian, P. et al. Adsorbate-induced shifts of electronic surface states: Cs on the (100) faces of tungsten, molybdenum, and tantalum. *Phys. Rev. B* **31**, 4911–4923 (1985).
42. Ozawa, K. et al. Potassium adsorption on the polar $\text{NbC}(111)$ surface: angle-resolved photoemission study. *Surf. Sci.* **375**, 250–256 (1997).
43. Ozawa, K. et al. Photoemission study of K adsorption on $\text{ZrC}(111)$. *Surf. Sci.* **433–435**, 700–704 (1999).
44. Zhang, S. et al. Time-resolved photoemission study of the electronic structure and dynamics of chemisorbed alkali atoms on $\text{Ru}(0001)$. *Phys. Rev. B* **93**, 045401 (2016).
45. Das, L. et al. Spin-orbital excitations in Ca_2RuO_4 revealed by resonant inelastic X-ray scattering. *Phys. Rev. X* **8**, 011048 (2018).
46. Gauquelin, N. et al. Pattern Formation by Electric-Field Quench in a Mott Crystal. *Nano Lett.* **23**, 7782–7789 (2023).
47. Sénéchal, D., Perez, D. & Plouffe, D. Cluster perturbation theory for hubbard models. *Phys. Rev. B* **66**, 075129 (2002).
48. Dagotto, E., Ortolani, F. & Scalapino, D. Single-particle spectral weight of a two-dimensional hubbard model. *Phys. Rev. B* **46**, 3183–3186 (1992).
49. Sekiyama, A. et al. Mutual experimental and theoretical validation of bulk photoemission spectra of $\text{Sr}_{1-x}\text{Ca}_x\text{VO}_3$. *Phys. Rev. Lett.* **93**, 156402 (2004).
50. Rodolakis, F. et al. Quasiparticles at the Mott transition in V_2O_3 : wave vector dependence and surface attenuation. *Phys. Rev. Lett.* **102**, 066805 (2009).
51. Yoshimatsu, K. et al. Dimensional-crossover-driven metal-insulator transition in SrVO_3 ultrathin films. *Phys. Rev. Lett.* **104**, 147601 (2010).
52. Takizawa, M. et al. Manifestation of correlation effects in the photoemission spectra of $\text{Ca}_{1-x}\text{Sr}_x\text{RuO}_3$. *Phys. Rev. B* **72**, 060404 (2005).
53. Panaccione, G. et al. Depth dependence of itinerant character in Mn-substituted $\text{Sr}_3\text{Ru}_2\text{O}_7$. *N. J. Phys.* **13**, 053059 (2011).
54. Fukazawa, H., Nakatsuji, S. & Maeno, Y. Intrinsic properties of the Mott insulator $\text{Ca}_2\text{RuO}_{4+\delta}$ ($\delta = 0$) studied with single crystals. *Phys. B Condens. Matter* **281**, 613–614 (2000).
55. Nakatsuji, S. & Maeno, Y. Synthesis and single-crystal growth of $\text{Ca}_{2-x}\text{Sr}_x\text{RuO}_4$. *J. Solid State Chem.* **156**, 26 – 31 (2001).

Acknowledgements

Fruitful discussion with M. Grioni is gratefully acknowledged. M. Horio, D.S., C.G.F., C.E.M., and J.C. acknowledge support by the Swiss National Science Foundation under grant no. 200021_188564. M. Horio and T.W. are supported by Grants-in-aid from the Japan Society of the Promotion of Science (JSPS) (grant No. 21K13872). M.K. was supported by KIAS Individual Grants (CG083501). This work was supported in part by the Italian Ministry of Foreign Affairs and International Cooperation, grant number KR23GR06. S.M. acknowledges support from the Swiss National Science Foundation under grant no. P300P2-171221. Y.S. is funded by the Swedish Research Council (VR) with a Starting Grant (Dnr. 2017-05078). G.S. acknowledges the hospitality of the Center for Computational Quantum Physics at the Flatiron Institute, a division of the Simons Foundation. G.S. and S.M. acknowledge funding support from the Deutsche Forschungsgemeinschaft (DFG, German Research Foundation) under Germany's Excellence Strategy through the Würzburg-Dresden Cluster of Excellence on Complexity and Topology in Quantum Matter ct.qmat (EXC 2147, Project ID 390858490) as well as through the Collaborative Research Center SFB 1170 ToCoTronics (Project ID 258499086). This research used resources from the Advanced Light Source, which is a DOE Office of Science User Facility under contract no. DE-AC02-05CH11231. We acknowledge Diamond Light Source for time at beamline I05 under proposal SI10550. We are grateful to the CPHT computer support team for the DFT +DMFT computation.

Author contributions

V.G., R.F., and A.V. grew the Ca_2RuO_4 single crystals. J.C. and H.M.R. conceived the ARPES project. M. Horio, D.S., C.G.F., C.E.M., S.M., Y.S., G.G., and J.C. carried out the ARPES experiments. The ARPES data were analyzed by M. Horio and D.S. M. Horio and T.W. conceived and performed the XPS experiments and analyzed the data. Photoemission beamlines were developed and maintained by M. Hoesch, T.K.K., S.M., C.J., A.B., E.R., and I.M. DMFT calculations were conducted by M.K., A.G., and G.S. Cluster-diagonalization calculations were carried out by F.F. and M.C. M.Horio, F.F., M.C., and J.C. wrote the manuscript with inputs from other authors.

Competing interests

The authors declare no competing interests.

Additional information

Supplementary information The online version contains supplementary material available at <https://doi.org/10.1038/s42005-023-01436-1>.

Correspondence and requests for materials should be addressed to Masafumi Horio or Filomena Forte.

Peer review information *Communications Physics* thanks the anonymous reviewers for their contribution to the peer review of this work. A peer review file is available.

Reprints and permission information is available at <http://www.nature.com/reprints>

Publisher's note Springer Nature remains neutral with regard to jurisdictional claims in published maps and institutional affiliations.



Open Access This article is licensed under a Creative Commons Attribution 4.0 International License, which permits use, sharing, adaptation, distribution and reproduction in any medium or format, as long as you give appropriate credit to the original author(s) and the source, provide a link to the Creative Commons license, and indicate if changes were made. The images or other third party material in this article are included in the article's Creative Commons license, unless indicated otherwise in a credit line to the material. If material is not included in the article's Creative Commons license and your intended use is not permitted by statutory regulation or exceeds the permitted use, you will need to obtain permission directly from the copyright holder. To view a copy of this license, visit <http://creativecommons.org/licenses/by/4.0/>.

© The Author(s) 2023